

# Long time mass fraction statistics in stationary compressible isotropic turbulence at supercritical pressure

Richard S. Miller<sup>a)</sup>

*Department of Mechanical Engineering, Clemson University, Clemson, South Carolina 29634-0921*

(Received 21 December 1999; accepted 3 May 2000)

Direct numerical simulations are used to investigate the “long time” distribution of mass fraction fluctuations in stationary compressible isotropic turbulent binary nitrogen–hydrocarbon mixtures under supercritical pressure conditions. The governing equations are the compressible Navier–Stokes equations together with the cubic Peng–Robinson real gas state equation, and generalized heat and mass diffusion derived from nonequilibrium thermodynamics. A highly efficient procedure is presented which allows for the solution of all thermodynamic quantities without iterations or interpolation tables. The simulations consider equal mass binary mixtures of various combinations of nitrogen, heptane, dodecane, and 3-methylhexane, having molecular weight ratios in the range  $1 \leq M_B/M_A \leq 6.08$ . It is shown that temperature and pressure-gradient-induced Soret mass diffusion results in statistically stationary mass fraction distributions at long times. The results reveal that the mass diffusion term due to the pressure gradient acts as a production mechanism in the Favre averaged scalar variance transport equation, and is balanced by Fickian dissipation to produce the stationary states. The resulting scalar probability density function is characterized by a larger than Gaussian flatness factor, and is asymmetric due to the mass fraction dependence of the partial molar volume. The stationary scalar variance amplitude increases both with increasing turbulence Mach number and molecular weight ratio of the species, but is inversely related to the turbulence Reynolds number. The scalar energy spectra exhibit peak values at wave numbers corresponding to the peak in the velocity dissipation spectra. © 2000 American Institute of Physics.  
[S1070-6631(00)00608-5]

## I. INTRODUCTION

A variety of modern air–fuel mixing and combustion devices operate under both transcritical and supercritical conditions, including gas turbines, diesel engines, and rocket engines. For example, typical hydrocarbon species have critical pressures  $\sim 15\text{--}30$  atm,<sup>1</sup> whereas diesel chambers reach pressures as large as  $\sim 60$  atm<sup>2</sup> after fuel ignition, and aircraft gas turbine combustor chambers operate at pressures  $\sim 30$  atm.<sup>3</sup> Above the critical point (or the mixture critical locus), real gas effects are prevalent and the distinction between gaseous and liquid phases vanishes; therefore, the phase of a supercritical substance is commonly referred to simply as “fluid.”<sup>1</sup> The majority of previous research on supercritical mixing considers single isolated droplets in quiescent environments. Typically oxygen–hydrogen systems are investigated under conditions relevant to rocket engines. The extent of this literature is too large to reference thoroughly in the present work; however, a recent review is given by Givler and Abraham.<sup>4</sup> High-pressure studies find that “vaporization” of supercritical “droplets” is dramatically altered from that under low-pressure conditions. In fact, in the absence of both phase change and latent heat effects, the process is entirely diffusional and the term vaporization is a misnomer. Even the term droplet is misleading since

under supercritical conditions there is no surface tension with which to maintain the sphericity of the fluid “blobs.”

High-pressure fluid formulations are nearly exclusively limited to spherically symmetric “droplet vaporization” in either the transcritical or supercritical regimes. Real gas effects are typically included through the use of cubic state equations such as the Peng–Robinson or Redlich–Kwong equations.<sup>1</sup> However, “irreversible” or “nonequilibrium”<sup>5</sup> thermodynamic effects from which species concentrations diffuse due to temperature gradients (Soret effect, or “thermal-diffusion”) and thermal energy diffuses due to concentration gradients (Dufour effect, or “diffusion-thermo”) are also known to be significant in real fluids,<sup>6–8</sup> particularly when large ratios of the molecular weights of the pure compounds are present.<sup>8</sup> Curtis and Farrell<sup>8</sup> were the first to include these effects in their treatment of supercritical droplets; however, their formulation incorrectly equated the Soret and Dufour diffusion coefficients and further neglected the “mass diffusion factor” which is related to molar gradients of the fugacity and can significantly alter the effective species diffusivity. Harstad and Bellan<sup>9–11</sup> later simulated high-pressure fluid droplets using a general diffusion flux formulation derived from fluctuation theory coupled with an efficient and accurate state equation.<sup>12</sup>

In contrast to laminar droplet studies, the extent of literature addressing turbulent high-pressure flows remains relatively limited. Experimental studies typically address fuel jets or atomizers issuing into high-pressure chambers, and

<sup>a)</sup>Electronic mail: rm@clemson.edu

are primarily based only on qualitative visualizations due to the inherent difficulties of making measurements in these environments.<sup>13–17</sup> Results show that the behavior of supercritical jets is dramatically altered from traditional low-pressure liquid jets. Low-pressure liquid-gas jets exhibit an initial pure liquid core which undergoes break up or atomization to form ligaments and droplets.<sup>18</sup> However, above the critical point the break up process ceases and behavior consistent with low-pressure gas-gas jets<sup>19</sup> is observed due to the absence of surface tension and latent heat.<sup>17</sup>

Oefelein and Yang<sup>20,21</sup> performed two-dimensional large eddy simulations (LES) of supercritical mixing layers with a Smagorinsky subgrid model, but did not consider Soret and Dufour diffusion. More recently, Miller *et al.*<sup>22,23</sup> included Soret and Dufour diffusion in their direct numerical simulations (DNS) of a temporally developing mixing layer composed of nitrogen and heptane streams. Their simulations primarily addressed the specification of the relatively poorly understood thermal diffusion factors which are related to the relative effects of Soret and Dufour diffusion. Two forms of the thermal diffusion factor appear in their formulation: the ‘‘Bearman–Kirkwood’’ and the ‘‘Irving–Kirkwood’’ forms. The two factors are related thermodynamically; however, one needs to be specified as a property of the particular species pairs under consideration. It was observed that specifying the Bearman–Kirkwood form of the thermal diffusion factor to be a small, constant ( $\sim 10^{-1}$ ) promotes relatively strong Dufour heat diffusion with limited Soret mass diffusion. On the other hand, an assumption of small constant Irinb–Kirkwood thermal diffusion factor creates the opposite effect; i.e., small Dufour effects with relatively substantial Soret effects. Comparison of experimental results with single droplet simulations suggests that specifying the Irving–Kirkwood thermal diffusion factor as a small constant yields the more physical behavior.<sup>11</sup>

The primary objective of the present study is to study the behavior of isotropic compressible turbulence of nitrogen–hydrocarbon mixtures under supercritical pressure conditions, including real gas and nonequilibrium diffusion effects. As a first investigation of this flow, the focus is primarily on the ‘‘long time’’ species mass fraction distribution which is found to evolve in a substantially different manner than in traditional low-pressure mixing studies. The mixing behavior is elucidated by conducting DNS of forced compressible isotropic turbulence of initially perfectly premixed binary mixtures. As will be shown, an eventual balance is achieved between dissipation and production mechanisms of the Fickian and Soret mass diffusion fluxes, resulting in an eventual stationary state for the mass fraction fields (with nonzero variance). In addition to the physical insight into nonequilibrium thermodynamic effects gained by studying this flow, the ultimate fate of the scalar field may also have significant impact on the potential for extending traditional combustion models, such as the amplitude mapping closure or probability density function (PDF) methods,<sup>24–27</sup> to high-pressure conditions.

The article is organized as follows: in Sec. II we describe the mathematical formulation of the governing equations, including the treatment of real gas effects and Soret

and Dufour diffusion. The numerical solution procedure is discussed in Sec. III. Results are presented in Sec. IV, followed by a final discussion and conclusions in Sec. V. Appendices are also provided with additional details of the formulation and solution procedure.

## II. MATHEMATICAL FORMULATION

The compressible form of the governing equations are derived for a binary mixture (denoted as species *A* and species *B*) of Newtonian fluids:

$$\frac{\partial \rho}{\partial t} + \frac{\partial}{\partial x_j} [\rho u_j] = 0, \quad (1)$$

$$\frac{\partial}{\partial t} (\rho u_i) + \frac{\partial}{\partial x_j} [\rho u_i u_j + p \delta_{ij} - \tau_{ij}] = \rho f_i, \quad (2)$$

$$\frac{\partial}{\partial t} (\rho e_t) + \frac{\partial}{\partial x_j} [(\rho e_t + p) u_j - u_i \tau_{ij} + Q_j] = \rho u_i f_i, \quad (3)$$

$$\frac{\partial}{\partial t} (\rho Y_B) + \frac{\partial}{\partial x_j} [\rho Y_B u_j + J_j] = 0, \quad (4)$$

where  $\rho$  is the density,  $u_i$  is the velocity,  $e_t = e_i + u_i u_i / 2$  is the total energy, i.e., internal energy ( $e_i$ ) plus kinetic energy,  $p$  is the thermodynamic pressure, and  $Y_B$  is the species *B* mass fraction (the species *A* mass fraction is  $Y_A = 1 - Y_B$ ). Furthermore,  $Q_j$  is the heat flux vector,  $J_j$  is the species *B* mass flux vector, and  $\tau_{ij}$  is the viscous stress tensor:

$$\tau_{ij} = \mu \left[ \frac{\partial u_i}{\partial x_j} + \frac{\partial u_j}{\partial x_i} - \frac{2}{3} \frac{\partial u_k}{\partial x_k} \delta_{ij} \right], \quad (5)$$

where  $\delta_{ij}$  is the Kronecker delta function and  $\mu$  is the mixture viscosity. Statistically stationary turbulence is maintained through the addition of a low-wave-number force vector  $f_i$  described later.

The cubic Peng–Robinson equation of state (EOS) is chosen to describe the nonideal thermodynamic state of the system:

$$p = \frac{\mathfrak{R}T}{V - \mathcal{B}_m} - \frac{\mathcal{A}_m}{V^2 + 2V\mathcal{B}_m - \mathcal{B}_m^2}, \quad (6)$$

where  $T$  is the temperature and  $\mathfrak{R}$  is the universal gas constant. The two (mixture) parameters specifying the EOS are

$$\mathcal{A}_m = \sum_{\alpha} \sum_{\beta} X_{\alpha} X_{\beta} \mathcal{A}_{\alpha\beta}, \quad \mathcal{B}_m = \sum_{\alpha} X_{\alpha} \mathcal{B}_{\alpha}. \quad (7)$$

In the above, the summations represent sums over both species (no summation over Greek indices hereinafter). The mole fraction of species  $\alpha$ ,  $X_{\alpha}$ , is related to the mass fraction by  $M_{\alpha} X_{\alpha} = M_m Y_{\alpha}$  where  $M_{\alpha}$  is the molecular weight of pure species  $\alpha$  and the mixture molecular weight is  $M_m = X_A M_A + X_B M_B$ . With this notation, the molar volume  $V$  is related to the density by  $V = M_m / \rho$ . The Peng–Robinson parameters  $\mathcal{A}_{\alpha\beta}$  and  $\mathcal{B}_{\alpha}$  are provided by an appropriate set of mixing rules which vary for different state equations and may have variations even for the same EOS. The mixing rules recommended by Harstad *et al.*<sup>12</sup> are implemented for this study and are provided in Appendix A. Cubic state equa-

tions are known to yield substantial predictive errors when compared to more complex forms of the EOS, particularly near the critical locus of a mixture.<sup>1</sup> However, the Peng–Robinson form has been tested and its volume predictions are within approximately 1% accuracy relative to the substantially more complex Lee–Kesler EOS<sup>1</sup> over the range of parameters considered in this study.

In linear nonequilibrium (or irreversible) thermodynamics, both the heat flux and mass flux vectors are assumed to be linear functions of gradients of the thermal and chemical potential functions.<sup>5</sup> The Onsager reciprocity relations, which derive from the time reversal invariance of the microscopic fluid description, form a set of relationships between the coefficients of the potential functions. This theory yields a form of the diffusion fluxes which naturally contains the ‘‘cross-diffusional’’ Soret and Dufour effects. A general form of the diffusion fluxes derived from fluctuation theory,<sup>28</sup> which is consistent with nonequilibrium thermodynamics,<sup>5</sup> has been derived previously.<sup>9–11,23</sup> Here, the heat ( $Q_i$ ) and mass ( $J_i$ ) fluxes are presented in a somewhat nontraditional form in order to simplify the following analyses:

$$Q_j = Q_j^T + Q_j^Y + Q_j^P, \quad (8)$$

$$J_j = J_j^T + J_j^Y + J_j^P, \quad (9)$$

where the superscripts indicate the thermodynamic spatial gradient involved. With this notation, the heat flux vector components are

$$Q_j^T = - \left\{ \kappa + \rho \mathcal{D} \alpha_{\text{IK}} \alpha_{\text{BK}} Y_A Y_B \mathfrak{R} \left( \frac{M_m}{M_A M_B} \right) \right\} \frac{\partial T}{\partial x_j}, \quad (10)$$

$$Q_j^Y = - \left\{ \rho \mathcal{D} \alpha_d \alpha_{\text{IK}} \mathfrak{R} T \left( \frac{M_m}{M_A M_B} \right) \right\} \frac{\partial Y_B}{\partial x_j}, \quad (11)$$

$$Q_j^P = - \left\{ \rho \mathcal{D} \alpha_{\text{IK}} Y_A Y_B \left( \frac{V_{,B}}{M_B} - \frac{V_{,A}}{M_A} \right) \right\} \frac{\partial p}{\partial x_j}, \quad (12)$$

and the mass flux vector components are

$$J_j^T = - \left\{ \rho \mathcal{D} \alpha_{\text{BK}} \frac{Y_A Y_B}{T} \right\} \frac{\partial T}{\partial x_j}, \quad (13)$$

$$J_j^Y = - \{ \rho \mathcal{D} \alpha_d \} \frac{\partial Y_B}{\partial x_j}, \quad (14)$$

$$J_j^P = - \left\{ \rho \mathcal{D} \frac{Y_A Y_B}{\mathfrak{R} T} \left( \frac{M_A M_B}{M_m} \right) \left( \frac{V_{,B}}{M_B} - \frac{V_{,A}}{M_A} \right) \right\} \frac{\partial p}{\partial x_j}, \quad (15)$$

where the molecular thermal conductivity is  $\kappa$  and the molecular mass diffusivity is  $\mathcal{D}$ . Note that the pressure-gradient-dependent terms ( $Q_j^P$  and  $J_j^P$ ) which result from the evaluation of the mixture chemical potential<sup>29</sup> are typically neglected in presentations of the Dufour and Soret diffusion fluxes. This is because the majority of studies typically address incompressible flows for which the thermodynamic pressure gradient is null.<sup>5</sup> However, the present investigation applies to compressible turbulence at moderate Mach numbers; therefore, the effects of thermodynamic pressure gradi-

ents cannot be neglected *a priori*. In fact, the results below will show that  $J_j^P$  plays a substantial role in the long time behavior of the mixing process.

In the above equations several new thermodynamic properties are introduced which are derived from the equation of state. The parameters  $\alpha_{\text{IK}}$  and  $\alpha_{\text{BK}}$  are referred to as the ‘‘Irving–Kirkwood’’ and the ‘‘Berman–Kirkwood’’ forms of the thermal diffusion factor<sup>30</sup> (discussed later). The mass diffusion factor,  $\alpha_d$ , is a thermodynamic parameter related to the fugacity coefficients:  $\alpha_d$  acts to alter the effective diffusivity ( $\mathcal{D}_{\text{eff}} = \mathcal{D} \alpha_d$ ) in the Fickian mass diffusion flux vector ( $J_i^Y$ ). Under ‘‘standard’’ low-pressure conditions  $\alpha_d \approx 1$ , whereas at the critical locus  $\alpha_d \rightarrow 0$ . The ‘‘effective’’ thermal conductivity appearing in the Fourier heat flux vector ( $Q_i^T$ ),

$$\kappa_{\text{IK}} = \kappa + \rho \mathcal{D} \alpha_{\text{IK}} \alpha_{\text{BK}} Y_A Y_B \mathfrak{R} \left( \frac{M_m}{M_A M_B} \right), \quad (16)$$

is referred to as the ‘‘Irving–Kirkwood’’ form of the thermal conductivity (denoted by  $\kappa_{\text{IK}}$ );<sup>30</sup> however, it is  $\kappa$  which is consistent with the conductivity derived from kinetic theory.<sup>31</sup> The partial molar volume is  $V_{,\alpha} = \partial V / \partial X_\alpha$  and the partial molar enthalpy is  $H_{,\alpha} = \partial H / \partial X_\alpha$ . These parameters obey the relations;  $V = \sum X_\alpha V_{,\alpha}$  and  $H = \sum X_\alpha H_{,\alpha}$  where the summations are over all species.<sup>29</sup> The thermodynamic parameters required for this study have been derived from the Peng–Robinson state equation and are provided in Appendix B.

The behavior of the Irving–Kirkwood ( $\alpha_{\text{IK}}$ ) and Berman–Kirkwood ( $\alpha_{\text{BK}}$ ) forms of the thermal diffusion factors<sup>22,23,30</sup> are poorly understood (particularly at high pressure); however, they are thermodynamically related:<sup>11</sup>

$$\alpha_{\text{IK}} = \alpha_{\text{BK}} + \frac{1}{\mathfrak{R} T} \left( \frac{M_A M_B}{M_m} \right) \left( \frac{H_{,B}}{M_B} - \frac{H_{,A}}{M_A} \right). \quad (17)$$

These nondimensional coefficients are related to the relative strength of the Soret and Dufour effects and are properties of the particular species pairs under consideration. Low-pressure kinetic theory suggests that  $\alpha_{\text{BK}}$  is  $\sim 10^{-1}$  and is nearly independent of the mass fraction (though it is in general a function of  $T$ ).<sup>31</sup> Miller *et al.*<sup>22,23</sup> investigated the effects of choosing constant values in the range  $10^{-2} \rightarrow 5$  for either of the thermal diffusion factors in their DNS of a temporal mixing layer. They observed that the second term on the right-hand side of Eq. (17) can be as large as  $\sim 10$ . Therefore, when  $\alpha_{\text{IK}}$  is assumed small and constant the Soret effects become pronounced whereas the Dufour effects are nearly negligible. The opposite effect was observed when  $\alpha_{\text{BK}}$  is assumed small and constant. However, calculations with the high-pressure droplet formulation<sup>11</sup> have been shown to compare most favorably with experimental results for heptane droplets in nitrogen environments when  $\alpha_{\text{IK}}$  is chosen to be a small positive constant  $\sim 10^{-1}$ .

### III. NUMERICAL APPROACH

A triply periodic three-dimensional ‘‘isotropic box turbulence’’ flow is considered in a cubic domain with equal lengths in each of the  $x_1$ ,  $x_2$ , and  $x_3$  coordinate directions

equal to  $L$ . Statistically stationary turbulence is achieved through a low-wave-number force vector added to the governing equations. The force vector  $f_i$  is constructed in physical space using the procedure described by Kida and Orszag<sup>32</sup> with only rotational components of the vector. For the present simulations the force takes the following form:

$$f_i = A_{ij} \sin(x_j/L_0) + B_{ij} \cos(x_j/L_0), \quad (18)$$

where  $L_0 = L/(2\pi)$  is the reference length scale, and each of the individual components of the amplitude tensors  $A_{ij}$  and  $B_{ij}$  are statistically independent, zero mean random variables having Gaussian distributions. The amplitudes of the off-diagonal elements of each tensor are characterized in terms of their standard deviations:

$$\overline{A_{ij}^2}^{1/2} = \overline{B_{ij}^2}^{1/2} = F_R = \frac{L_0}{a_0} F_R^* \quad (i \neq j), \quad (19)$$

where the overbar indicates the temporal averaging operator, and the force amplitude is nondimensionalized as  $F_R^* = F_R a_0^2 / L_0$  where  $a_0$  is a reference velocity scale. Compressive contributions to the force vector are not considered so that the diagonal tensor elements are null; i.e.,  $A_{ij} = B_{ij} = 0$  for all  $i = j$ .

In general, cubic real gas state equations cannot be solved in a completely noniterative manner in the context of compressible Navier–Stokes simulations. At each grid point and time step the density, the internal energy, and the mass fractions are known (the molar volume is therefore also known). Obtaining both the temperature and the pressure simultaneously requires iterating the state equation together with its corresponding expression for internal energy (the molar internal energy is  $E = H - pV$ ; see Appendix B). Unfortunately, performing iterations at each grid point and time step is overly taxing for three-dimensional DNS. Previous two-dimensional simulations<sup>20,21</sup> based on using *a priori* constructed thermodynamic tables requiring interpolations are also computationally intensive. In order to overcome this problem, Miller *et al.*<sup>22,23</sup> developed an efficient procedure applicable to a binary nitrogen–heptane mixture in which a highly accurate three-dimensional curve fit is constructed within a specified range of thermodynamic state space (i.e., *a priori* specified ranges of  $T$ ,  $p$ , and  $Y_B$ ). The curve fit provides the temperature explicitly as a function of the density, heptane mass fraction, and the internal energy, all of which are known in the context of the DNS. Given the temperature, the state equation can then be solved explicitly for the pressure. The primary limitation of their methodology is that a specific curve fitting function was produced, and is only valid for the binary nitrogen–heptane mixture. Expanding the procedure to either different species or a different range of state space would therefore require recalculating the fitting parameters, and possibly choosing a new form for the fitting functions.

In the present paper, we introduce an improved methodology in which a more general set of functions is employed, and all parameters are calculated based on least mean square error (LMSE) analysis. The only inputs required for the model are the critical properties and molecular weights of the

species pairs required for the state equation. This procedure enables substantially more robust and accurate curve fits for arbitrary species pairs, and is also found to allow for the consideration of a broader range of thermodynamic state space without loss of accuracy. Because the LMSE procedure is employed to find the coefficients, the corresponding calculations can be performed within the DNS code during initialization and are therefore completely transparent to the user. Furthermore, the range of state space can also be expanded dynamically during a simulation if the actual conditions are found to exceed the original bounds. The specifics of the new curve fitting procedure are presented in Appendix C.

The governing equations are solved numerically on a uniformly spaced computational mesh using a third-order-accurate explicit Runge–Kutta temporal integration and eighth order accurate central finite differences to discretize all spatial derivatives.<sup>33</sup> As recommended in Ref. 33, a tenth order explicit (minimal) filtering is also applied to each of the primitive variables at every Runge–Kutta stage in order to control potential numerical instabilities. In practice, the time step is calculated at every iteration using the minimum of values calculated using both a velocity based Courant number equal to  $\frac{7}{10}$  and a diffusion based Courant number equal to  $\frac{1}{10}$ . The code is parallelized based on three-dimensional domain decomposition, using the Message Passing Interface (MPI) subroutines for all interprocessor communications. The simulation time requirement is approximately 6.9 sec per iteration for a resolution of  $128^3$  grid points running on 64 processors on a Hewlett Packard Convex Exemplar supercomputer. The code is an expanded version of the well-tested code used by Miller and Bellan<sup>34</sup> to study the low-pressure, two-phase temporally developing mixing layer. Further validation of the code was made through comparisons (under low-pressure conditions) with previous results of Kida and Orszag<sup>32</sup> for forced isotropic turbulence. These comparisons (together with additional results presented later) confirm the accuracy of the numerical approach.

#### IV. PROPERTIES

In the context of a DNS simulation we are not interested in exactly matching the true values of the diffusion coefficients since the resulting Reynolds numbers would be far too large to resolve with realistic length scales. In addition, for the purposes of this study we wish to simplify the treatment of the diffusion coefficients in order to highlight the effects of the real gas state equation and the Soret and Dufour diffusion effects. We therefore adopt a constant viscosity calculated from a specified value of the flow Reynolds number,  $Re_0$  (defined below). In a similar manner, the Prandtl number [ $Pr = \mu / (\rho C_p k)$ ] and Schmidt number [ $Sc = \mu / (\rho D)$ ] are chosen to be constants  $Pr = Sc = 0.7$  (unity Lewis number). Accepting the fact that the behavior of the thermal diffusion factors is poorly understood, particularly at high pressures, we choose to use a previously published (low-pressure) empirical correlation to specify  $\alpha_{IK}$  in terms of the molecular weight ratio:<sup>8</sup>

TABLE I. Simulation parameters and initial conditions. All simulations are initialized with uniform distributions of mass fraction, temperature, and pressure;  $Y_B=0.5$ ,  $T_0=700$  K, and  $p_0=45$  atm, respectively.

Run	Species A	Species B	$N^3$	$Re_0$	$F_R^*$	$M_B/M_A$	$\alpha_{IK}$	$\rho_0$ (kg/cm <sup>3</sup> )	$a_0$ (m/sec)
1	Nitrogen	Heptane	64 <sup>3</sup>	75	0.05	3.58	0.161	33.9	389.4
2	Nitrogen	Heptane	128 <sup>3</sup>	450	0.05	3.58	0.161	33.9	389.4
3	Nitrogen	Heptane	128 <sup>3</sup>	150	0.35	3.58	0.161	33.9	389.4
4	Heptane	3-Methylhexane	128 <sup>3</sup>	450	0.05	1.0	0.024	94.4	214.5
5	Nitrogen	Dodecane	128 <sup>3</sup>	450	0.05	6.08	0.218	37.1	371.7

$$\alpha_{IK} = 2.3842 \times 10^{-2} + 0.24821 \log_{10}(M_B/M_A), \quad (20)$$

for  $M_B/M_A \geq 1$ . The Bearman–Kirkwood form ( $\alpha_{BK}$ ) is then thermodynamically determined by Eq. (17). Finally, the reference heat capacity  $C_p^0$  is evaluated at a ‘‘low-pressure’’ reference condition as generally employed in the departure function formalism.<sup>1</sup> The reference heat capacity and the reference enthalpy ( $H^0$ ) of the mixture are specified in terms of the pure substance reference values:

$$C_p^0 = X_A C_{p,A}^0 + X_B C_{p,B}^0, \quad H^0 = X_A H_A^0 + X_B H_B^0. \quad (21)$$

The reference pressure is chosen to be  $p^0 = 1$  atm, and the pure substance reference heat capacities ( $C_{p,A}^0$  and  $C_{p,B}^0$ ) are taken from polynomial correlations in Ref. 1. Finally, the pure species reference enthalpies ( $H_A^0$  and  $H_B^0$ ) are obtained by integrating the  $C_{p,A}^0$  and  $C_{p,B}^0$  correlations with assumed zero reference enthalpy at zero temperature (this is valid in the absence of phase changes).<sup>35</sup>

## V. RESULTS

The parameters used for the simulations conducted in this study are presented in Table I. All simulations are performed for binary mixtures, typically nitrogen with various hydrocarbons. The species are initialized as perfectly premixed, with equal masses of each species within the cubic domain (i.e.,  $Y_A = Y_B = \frac{1}{2}$  everywhere). The initial temperature and pressure are also uniform throughout the domain and are  $T_0 = 700$  K and  $p_0 = 45$  atm for all simulations. These conditions are chosen due to their relevance to both diesel engines<sup>2</sup> and gas turbines.<sup>3</sup> The velocity field is in all cases initialized as quiescent ( $u_i \equiv 0$ ). The speed of sound and density are therefore initially uniform throughout the domain and are chosen as the reference velocity and density scales,  $a_0$  and  $\rho_0$ , respectively. The flow Reynolds number based on these scales is defined as  $Re_0 = \rho_0 a_0 L_0 / \mu$ .

The simulation parameters listed in Table I are chosen in order to study the effects of the molecular weight ratio of the species, the turbulence Reynolds number, and the turbulence Mach number. For each simulation, Table I provides the binary species, the grid resolution, the flow Reynolds number, the nondimensional forcing amplitude, and the ratio of molecular weights of the species. Furthermore, the initial values of the Irving–Kirkwood form of the thermal diffusion factor, and the reference density and velocity (sound speed), are also included in the table. Runs 2, 4, and 5 are used to assess the effects of the species molecular weight ratio in the range  $1.0 < M_B/M_A < 6.08$ . The parameters for runs 1 and 2 are

adopted to address Reynolds number effects, and those of runs 2 and 3 address Mach number effects (described later).

The molecular weights of the species as well as the critical and reduced initial values of the pure substance temperatures and pressures are given in Table II. Nitrogen is chosen as a pure species having properties similar to those of air. The hydrocarbons chosen are dodecane, heptane, and 3-methylhexane. These species are chosen to be representative of typical hydrocarbon fuels of the type which are liquid under standard conditions. Heptane and 3-methylhexane are essentially equivalent thermodynamically. These two species are used to simulate a mixture having  $M_B/M_A = 1$  (run 4) as a baseline comparison for the remaining simulations. Note that the initial conditions are chosen such that only purely supercritical conditions are considered for the pure species. Analysis of the thermodynamic state space and the simulation results indicates that the mixtures also remain supercritical for all simulations. This removes the substantially increased difficulties associated with treating the transcritical regime in which (gas–liquid) phase change surfaces can appear. Such surfaces would need to be tracked accurately (in a Lagrangian manner) in order to account for vaporization or condensation, as well as latent heat effects. However, these issues are beyond the subject of the present research and will not be addressed hereinafter.

## A. Stationary flow states

As the simulations commence, the solenoidal force ( $f_i$ ) begins to ‘‘stir’’ the initially quiescent fluid mixtures leading to quasi-stationary turbulent flows. The fully developed flows can only be considered ‘‘quasi-’’ stationary due to the fact that dissipation of turbulence energy results in a production of internal energy in the compressible formulation.<sup>32</sup> In this case, the mean temperature (and pressure) within the domain increase with time as energy is continuously added to the system via the forcing. The temporal evolutions of the volume-averaged flow temperatures are shown in Fig. 1 for

TABLE II. Pure substance properties and reduced initial conditions.

Species	$M$ ( $\frac{\text{kg}}{\text{kg}\cdot\text{mole}}$ )	$T^c$ (K)	$p^c$ (atm)	$T_0/T^c$	$P_0/P^c$
Nitrogen	28.013	126.26	33.46	5.54	1.34
Heptane	100.205	540.3	27.04	1.30	1.66
3-Methylhexane	100.205	535.3	27.73	1.31	1.62
Dodecane	170.34	658.2	17.96	1.06	2.51

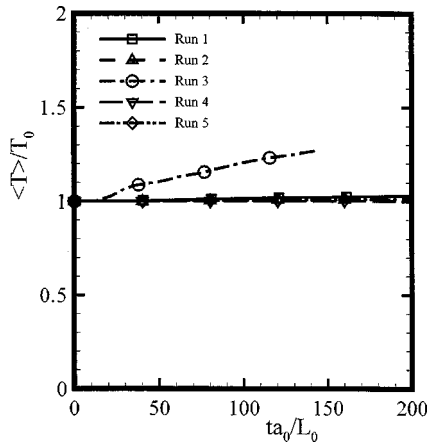


FIG. 1. Temporal evolution of the nondimensional mean temperature.

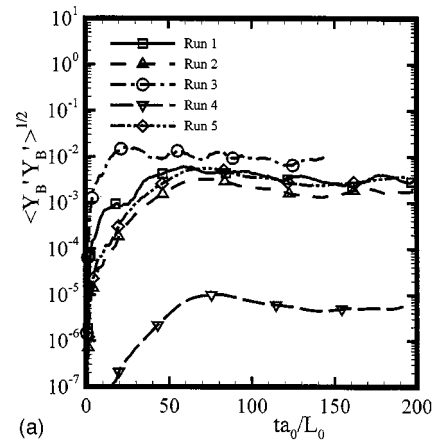
all simulations. With the exception of run 3 the relative increase in the mean temperatures are relatively small, with the absolute mean temperatures increasing to no greater than approximately 720 K (from  $T_0 = 700$  K). In the case of run 3, the mean temperature increases by approximately 27% over the duration of the simulation (to  $\approx 890$  K) due to a larger forcing amplitude and viscosity. Nevertheless, the relative changes to the thermodynamic properties corresponding to this temperature interval were found to be relatively moderate. Therefore, all of the flows are considered to be essentially stationary for the purposes of the following analyses (the approximate stationarity of the flows is further confirmed by analyses of higher-order statistical quantities, e.g., Figs. 2 and 3).

Statistics are calculated as both instantaneous volume averages over the entire domain, as well time averages of data made possible by the stationarity of the flows. The flow stationarity and the resulting ability to calculate time average statistics (by ergodicity) eliminates the need to perform multiple realizations of each simulation; therefore, each of runs 1–5 in Table I corresponds to a single realization. The volume average of arbitrary variable  $\phi$  is denoted by brackets  $\langle \phi \rangle$ , and the fluctuation with respect to the average is denoted with a superscript prime; i.e.,  $\phi' = \phi - \langle \phi \rangle$ . Several time-averaged statistics are presented in Table III for each of the simulations. The averages are performed over the time range  $100 \leq ta_0 / L_0 \leq 200$  for all flows, except for run 3 which develops more rapidly in nondimensional time units. For run 3 the averaging is performed for the temporal range  $50 \leq ta_0 / L_0 \leq 150$ . The statistics presented in Table III are calculated in forms suitable to isotropic compressible flow.<sup>32</sup> The Mach number is  $M_C = \langle u_i u_i \rangle^{1/2} / a$ , and the Taylor Reynolds number is

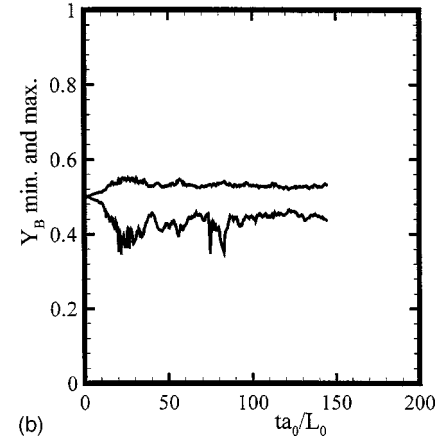
$$\text{Re}_\lambda = \langle \rho \rangle \langle u_i u_i \rangle \left( \frac{5}{3\mu\varepsilon} \right)^{1/2}, \quad (22)$$

where the mean dissipation can be written as a summation of solenoidal ( $\varepsilon_S$ ) and compressive ( $\varepsilon_C$ ) components; i.e.,  $\varepsilon = \varepsilon_S + \varepsilon_C$  with

$$\varepsilon_S = \mu \langle \omega_i \omega_i \rangle, \quad \varepsilon_C = \frac{4}{3} \mu \left\langle \frac{\partial u_i}{\partial x_i} \right\rangle \quad (23)$$



(a)



(b)

 FIG. 2. Temporal evolution of the species  $B$  mass fraction (a) standard deviation for all simulations, and (b) instantaneous maximum and minimum for simulation run 3.

( $\omega_i$  is the vorticity vector). The Taylor ( $\lambda$ ) and Kolmogorov ( $\eta$ ) length scales are defined as

$$\lambda = \left( \frac{5\mu \langle u_i u_i \rangle}{\varepsilon} \right)^{1/2}, \quad \eta = \left( \frac{\mu^3}{\varepsilon \langle \rho \rangle^2} \right)^{1/4}, \quad (24)$$

respectively. Finally, the time-averaged compressibility ( $Z = pV/\mathfrak{R}T$ ), mass diffusion factor ( $\alpha_d$ ), Bearman–Kirkwood thermal diffusion factor ( $\alpha_{BK}$ ), and the relative Irving–Kirkwood form of the thermal conductivity ( $\kappa_{BK}/\kappa$ ) are also presented.

The statistics provided in Table III reveal why the particular values of the flow Reynolds numbers and forcing amplitudes were chosen. The particular choices enable us to study the effects of altering either the turbulence Reynolds number or the Mach number while keeping the remaining parameters essentially fixed. The simulations are performed for both ‘‘low’’ and ‘‘moderate’’ Reynolds numbers equal to  $\text{Re}_\lambda \approx 16$  (run 1) and  $\text{Re}_\lambda \approx 52$  (runs 2–5), respectively. Two values of the turbulence Mach number are also considered,  $M_C \approx 0.21$  (runs 1, 2, 4, and 5) and  $M_C \approx 0.56$  (run 3). The larger  $M_C$  value is sufficient to exhibit significant compressibility effects; however, it is not large enough to produce shocklets<sup>36</sup> within the flow which would be poorly resolved by the nondissipative central finite differences employed in this study. Table III also reveals that the Kolmogorov length

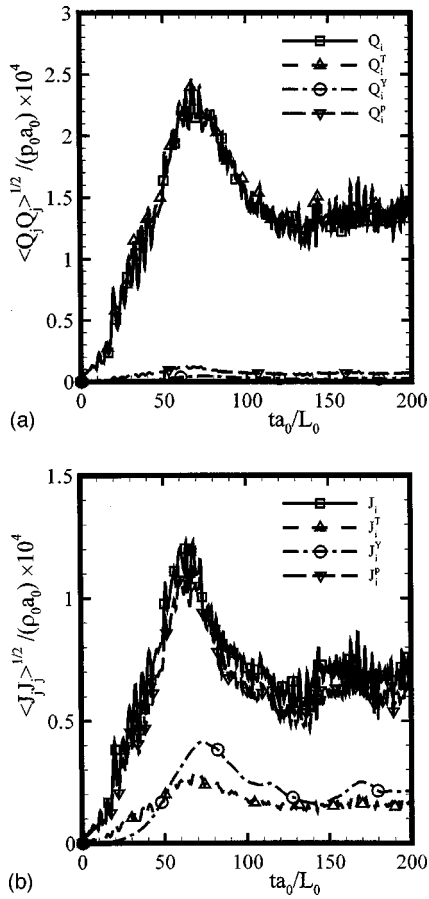


FIG. 3. Temporal evolution of the nondimensional (a) heat and (b) mass flux vector magnitudes for simulation run 2.

scale is in all cases significantly larger than the grid spacing, suggesting that the simulations are well resolved. The integrity of the simulations was further confirmed through reproduction of (low-pressure) results in Ref. 32 (not shown), and through examination of the high-wave-number content of various energy spectra (presented below).

The statistics of thermodynamic variables in Table III yield additional insight into the behavior of the simulated flows. Pure hydrocarbons under the present conditions exhibit considerable deviations from ideal gas behavior. For example, the compressibilities of pure heptane and dodecane at  $p = p_0$  and  $T = T_0$  are  $Z = 0.81$  and  $Z = 0.46$ , respectively. However, dilution with nitrogen ( $Z = 1.04$ ) as in runs 1–3 and run 5 results in mean compressibilities very near to unity. In other words, the mixture compressibility is a nonlinear function of the mass fractions of the species, and 50% dilution with a compressible hydrocarbon actually retains the

TABLE III. Time-averaged statistics.

Run	$M_C$	$Re_\lambda$	$\lambda/L_0$	$\eta/\Delta x$	$Z$	$\alpha_d$	$\alpha_{BK}$	$\kappa_{IK}/\kappa$
1	0.21	16.1	1.61	2.10	1.02	0.914	-5.27	0.992
2	0.20	51.1	0.91	1.32	1.02	0.910	-5.13	0.990
3	0.56	54.8	0.96	1.34	1.02	0.937	-6.99	0.986
4	0.21	52.2	0.91	1.31	0.84	0.926	-0.13	1.00
5	0.20	51.5	0.92	1.34	1.02	0.817	-7.70	0.986

near ideal compressibility associated with pure nitrogen. On the other hand, run 4 is comprised of a binary mixture of two hydrocarbons and is substantially more “liquid-like” as characterized by a less than unity compressibility  $Z \approx 0.84$ . In all cases, the magnitude of the fluctuations of the compressibility are much less than the mean values, i.e.,  $\langle (Z')^2 \rangle^{1/2} \ll \langle Z \rangle$ , and are not shown. As discussed previously, the mass diffusion factor ( $\alpha_d$ ) acts to alter the effective Fickian diffusivity when its value is different than unity. Table III shows that the mean  $\alpha_d$  is indeed significantly less than unity for all flows. Thermodynamic conditions for the simulations were chosen to be sufficiently far from the critical mixture locus (where  $\alpha_d \rightarrow 0$ ) such that the scalar field remains well resolved. In this regard, the largest effective Schmidt number occurs for run 5;  $Sc_{\text{eff}} = \mu / (\rho D \alpha_d) = Sc / \alpha_d \approx 0.86$ . The average Bearman–Kirkwood thermal diffusion factor ( $\alpha_{BK}$ ) reveals that the magnitude of the second term on the right-hand side of Eq. (17) is much larger than the specified values of  $\alpha_{IK}$  (see Table I). Finally, the last column in Table III shows that the effective thermal conductivity (the Irving–Kirkwood form) is approximately equal to the “true” (i.e., kinetic theory) value of the molecular conductivity. Therefore, the second term in the brackets in Eq. (10) is negligible for the present flow conditions and  $Q_j^T$  is nearly identical to the traditional Fourier form of the heat flux vector.

## B. Scalar evolution

Under the typical low-pressure formulation in which mass diffusion is purely Fickian, the initially premixed species would remain perfectly mixed indefinitely. This is not the case for the present formulation due to the inclusion of Soret mass diffusion whereby species also diffuse due to temperature and pressure gradients. In the absence of initial species gradients, temperature and pressure gradients inherent in compressible turbulence initially act to generate fluctuations in the mass fraction fields (the production mechanism is described in more detail below). The relative intensity of fluctuations of some variable  $\phi$  can be examined in terms of the standard deviation of  $\phi$  defined as  $\langle \phi' \phi' \rangle^{1/2}$ . Figure 2 depicts the temporal evolutions of the standard deviations of the species  $B$  mass fractions for all simulations [Fig. 2(a)], as well as the evolutions of the instantaneous minima and maxima of  $Y_B$  for simulation run 3 [Fig. 2(b)]. It is observed that the species mass fraction fields also evolve to statistically stationary distributions as characterized by the scalar standard deviations [the relative magnitudes in Fig. 2(a) are discussed later]. Although the standard deviations are relatively small compared to the scalar mean ( $\langle Y_B \rangle = \frac{1}{2}$ ), the magnitude of the fluctuations is not negligible as observed by the minima and maxima in Fig. 2(b). Additional simulations have been conducted based on perfectly segregated (non-premixed) nitrogen–hydrocarbon initial conditions. These results confirm that the long time stationary scalar states observed in Fig. 2 are independent of the mass fraction initial conditions (not shown).

The relative effects of the Dufour and Soret cross-diffusion on the heat and mass flux vectors are examined in Fig. 3 which depicts the magnitudes of all four vectors in

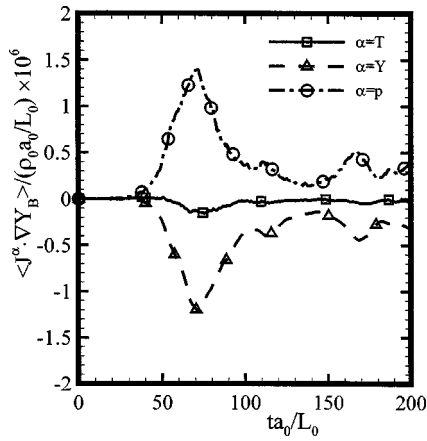


FIG. 4. Temporal evolution of the nondimensional species  $B$  mass fraction variance transport equation budget for simulation run 2.

each of Eqs. (8) and (9), i.e., the total flux together with each of the temperature, mass fraction, and pressure-gradient-dependent component contributions. Note also that with these definitions the summation of the three component magnitudes does not necessarily equal the magnitude of the total flux vector. The results in Fig. 3 correspond to simulation run 2 (although the trends are the same for the remaining flows), and the high-frequency oscillations in the curves are due to acoustic waves. Figure 3(a) shows that the total ( $Q_i$ ) and temperature-gradient-dependent ( $Q_i^T$ ) heat flux vector magnitudes are approximately equal, whereas the cross-diffusion (Dufour effect) vectors ( $Q_i^Y$  and  $Q_i^p$ ) are essentially negligible at all times. On the other hand, Fig. 3(b) reveals that the relative magnitudes of the cross-diffusion mass flux vectors (Soret effect) are substantial for the presently investigated stationary flows. In fact, the pressure-gradient-dependent mass flux ( $J_i^p$ ) makes an even larger contribution to the total mass flux vector than does the “typical” Fickian flux ( $J_i^Y$ ).

The mechanisms responsible for the observed stationary mass fraction states for the high pressure binary mixtures can be explained by examining the transport equation for the Favre averaged mass fraction variance for isotropic flow:

$$\frac{d}{dt} \left( \langle \rho \rangle \frac{\overline{Y_B'' Y_B''}}{2} \right) = \left\langle J_j^T \frac{\partial Y_B}{\partial x_j} \right\rangle + \left\langle J_j^Y \frac{\partial Y_B}{\partial x_j} \right\rangle + \left\langle J_j^p \frac{\partial Y_B}{\partial x_j} \right\rangle, \quad (25)$$

where the density-weighted Favre average of arbitrary variable  $\phi$  is denoted  $\tilde{\phi}$  and the corresponding fluctuation is  $\phi'' = \phi - \tilde{\phi}$  (see Ref. 37 for a discussion of the relationship between the nonweighted and the Favre-averaged scalar variance). Clearly, the second term on the right-hand side due to  $J_j^Y$  is negative definite and therefore corresponds to the traditional Fickian dissipation of scalar variance. However, the physical interpretation of the remaining terms is less obvious since their sign will depend upon the correlations of the mass fraction gradient with either  $J_j^T$  or  $J_j^p$ . In order to gain insight into the behavior of these terms, the evolution of the scalar variance budget is presented in Fig. 4 for simulation run 2. The positive values for  $\langle J_j^p \partial Y_B / \partial x_j \rangle$  indicate that the pres-

TABLE IV. Time-averaged correlation coefficients.

Run	$C(T, Y_B)$	$C(p, Y_B)$	$C(\nabla T, \nabla Y_B)$	$C(\nabla p, \nabla Y_B)$
1	0.034	0.53	0.02	0.51
2	-0.004	0.35	-0.13	0.44
3	0.007	0.33	-0.10	0.33
4	-0.028	-0.21	0.17	-0.26
5	-0.12	0.36	-0.28	0.45

sure gradient dependent Soret flux ( $J_i^p$ ) acts as a production mechanism for mass fraction fluctuations. On the other hand, although the temperature-gradient-dependent flux ( $J_i^T$ ) is relatively strong, as indicated in Fig. 3(b),  $J_i^T$  plays a relatively negligible role in the long time variance budget. In other words, Soret effects from temperature gradients may be important locally within the flow; however, the averaged effect on the scalar variance equation is negligible due to a lack of correlation between the temperature and mass fraction gradients (see also Table IV).

Based on the above description, it can be concluded that the initial perfect “premixedness” of the mass fraction field is broken (“anti-diffusion”) by the effects of pressure and temperature gradients within the flow acting on the mass diffusion vector. On average, the pressure gradient acts to increase the scalar variance until a balance is achieved between the production effects associated with  $J_j^p$  and the dissipation due to the Fickian diffusion term. This balance is manifested in long time statistically stationary mass fraction distributions. Furthermore, since the pressure gradient acts as the primary scalar variance production mechanism, it can be expected that the mass fraction gradient and the pressure gradient will be correlated. This is confirmed by introducing the correlation coefficient for two vectors  $a_i$  and  $b_i$ :

$$C(a_i, b_i) = \frac{\langle a_i b_i \rangle}{(\langle a_j a_j \rangle \langle b_k b_k \rangle)^{1/2}}, \quad (26)$$

bounded by  $-1 \leq C \leq +1$ . Time-averaged correlation coefficients for the mass fraction gradient with both the temperature and pressure gradients are provided in Table IV. As expected, the mass fraction and pressure gradients are significantly correlated, whereas the mass fraction and temperature gradients exhibit only relatively negligible correlations. These correlations are direct measures of the relative Soret effects on the scalar variance transport equation. Table IV also includes correlations for the scalar values (as opposed to the gradients). For scalars, the correlation coefficient is defined in an analogous manner:

$$C(\phi_1, \phi_2) = \frac{\langle \phi_1' \phi_2' \rangle}{\langle (\phi_1')^2 \rangle^{1/2} \langle (\phi_2')^2 \rangle^{1/2}}. \quad (27)$$

Similar trends are observed for the scalar correlations. Finally, note that the change in the sign for correlations calculated for run 4 are due only to the choice of the pure substance referred to as species  $B$ .

TABLE V. Time-averaged standard deviation, skewness, and flatness for the species  $B$  mass fraction.

Run	$\langle (Y'_B Y'_B)^{1/2} \rangle$	$\mu_3(Y_B)$	$\mu_4(Y_B)$
1	$3.50 \times 10^{-3}$	-0.39	3.56
2	$1.85 \times 10^{-3}$	-1.57	7.52
3	$9.75 \times 10^{-3}$	-1.06	5.56
4	$6.0 \times 10^{-6}$	1.60	7.27
5	$3.2 \times 10^{-3}$	-1.75	9.04

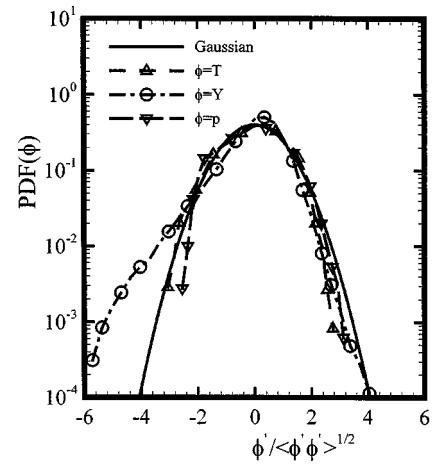
### C. Scalar distribution

The long time concentration fluctuations resulting from nonequilibrium diffusion may have significant consequences for the extension of standard PDF-based mixing models (e.g., the amplitude mapping closure or PDF methods<sup>24–27</sup>) to high-pressure conditions. It is therefore warranted to further investigate the ultimate form of the scalar distributions. The temporal evolutions of the mass fraction standard deviations were already presented in Fig. 2(a). Their corresponding time averaged values are provided in Table V, together with the time-averaged skewness ( $\mu_3$ ) and flatness ( $\mu_4$ ) factors:

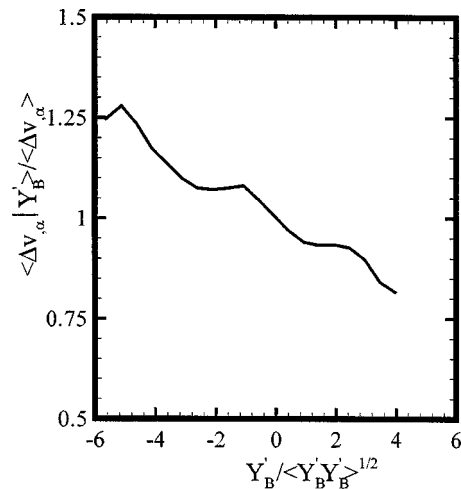
$$\mu_n(Y_B) = \frac{\langle (Y'_B)^n \rangle}{\langle (Y'_B)^2 \rangle^{n/2}}, \quad (28)$$

which take values  $\mu_3=0$  and  $\mu_4=3$  for Gaussian statistics. Substantial variations in the intensity of the scalar fluctuations are observed for the different simulations. An analysis of the results shows that the mass fraction standard deviations increase with each of the following trends; (i) increases in the molecular weight ratio of the pure species (runs 4, 2, and 5), (ii) increases in the mixture viscosity (i.e., decreasing  $Re_\lambda$ ; runs 1 and 2), and (iii) increasing Mach number (runs 2 and 3). One effect of decreasing the molecular weight ratio is to reduce the partial molar volume difference in Eq. (15). This reduces the relative strength of  $J_i^p$ , and therefore also reduces the production of scalar variance [Eq. (25)]. The viscosity is directly related to both the thermal conductivities and the mass diffusivities of the mixtures through the specified values of the Prandtl and Schmidt numbers. Therefore, the increasing scalar variances with viscosity are most simply explained by considering the limiting case of zero conductivity and diffusivity; in this case the mass flux vector is null and no scalar production can occur. However, despite the trends found in Table III for increasing Reynolds number, the ultimate asymptotic state of the scalar distributions with large, but finite, Reynolds number is not certain. Finally, analyses of the results shows that the increase of the scalar variance with Mach number is due to a corresponding increase in the intensity of the pressure fluctuations which govern the scalar variance production.

Table V also indicates that all of the distributions are characterized by substantial skewness values and larger than Gaussian flatness factors. An example of an instantaneous mass fraction normalized PDF is given in Fig. 5 together with PDFs of the temperature and pressure fluctuations for simulation run 3. The species  $B$  mass fraction is clearly skewed towards negative fluctuation values. This is in con-

FIG. 5. Probability density functions of normalized thermodynamic variable fluctuations for simulation run 3 at time  $ta_0/L_0=125$ .

trast to “typical” low-pressure passive scalar distributions which tend to be predominantly symmetric and approximately Gaussian.<sup>38,39</sup> However, both the temperature and the pressure are nearly Gaussian (indicated by the solid curve). The scalar skewness is therefore not due to skewness in either the pressure or temperature gradient distributions. Analyses of the results indicate that the mass fraction skewness is due to the thermodynamic properties of the partial molar volume difference which appears in the mass flux vector  $J_i^p$  [Eq. (15)]. Figure 6 elucidates this feature by averaging the partial volume difference,  $\Delta v_{,\alpha} = (V_{,B}/M_B - V_{,A}/M_A)$ , conditionally on the value of the species  $B$  mass fraction. Clearly, the partial volume difference is a decreasing thermodynamic function of the mass fraction. Therefore, the flux vector magnitude  $J_i^p$  is larger in regions of negative  $Y_B$  fluctuations, and the production of scalar fluctuations is correspondingly larger in these areas. This increases the probability of finding small values of  $Y_B$  leading to the observed skewness [also compare the minima and maxima in Fig. 2(b)]. Conversely, species  $A$  exhibits positive skewness

FIG. 6. Nondimensional conditional expectation of the partial molar volume difference  $\Delta v_{,\alpha} = (V_{,B}/M_B - V_{,A}/M_A)$  conditioned on the species  $B$  mass fraction fluctuation for simulation run 3 at time  $ta_0/L_0=125$ .

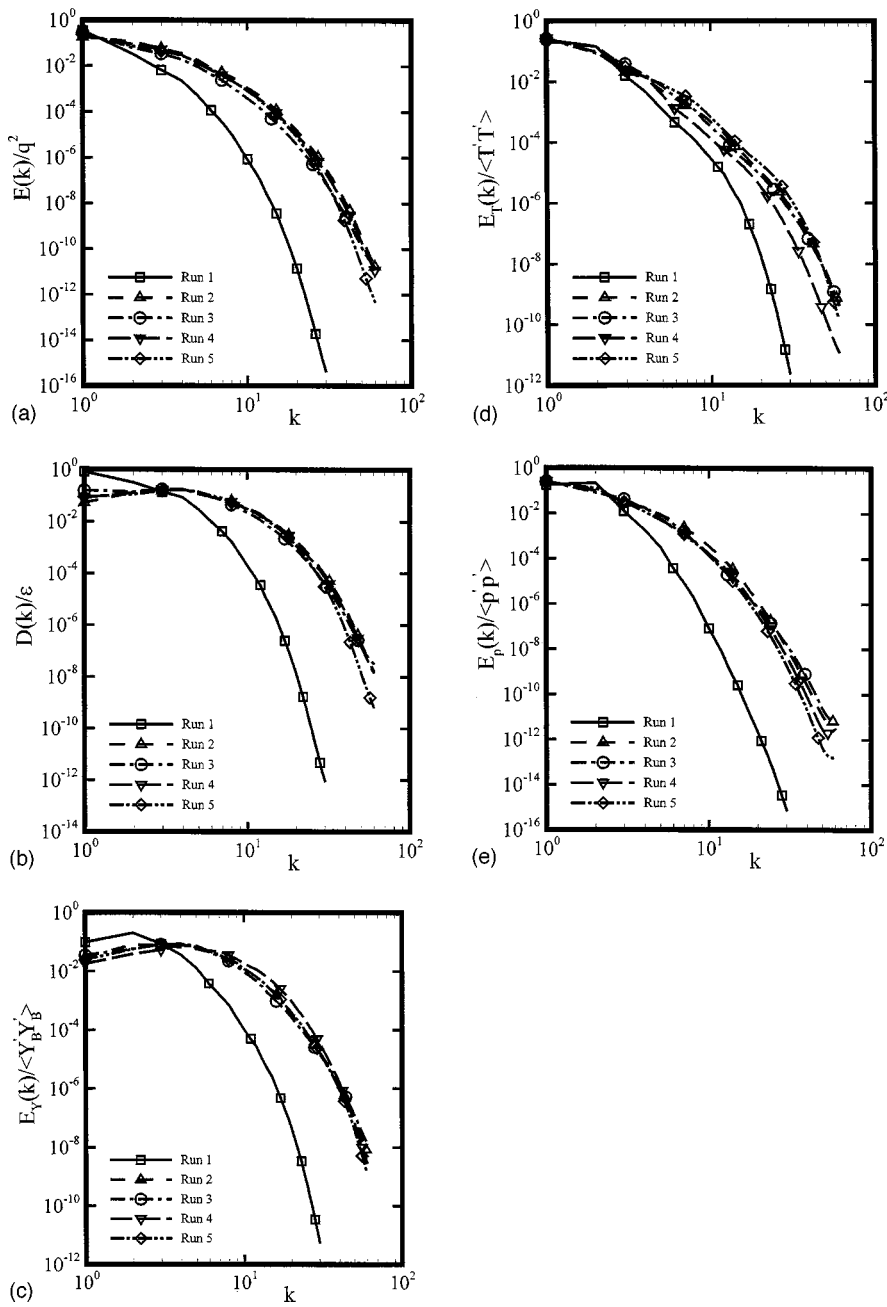


FIG. 7. Nondimensional fluctuation energy spectra as a function of the wave number magnitude for all simulations: (a) kinetic energy, (b) dissipation of kinetic energy, (c) species  $B$  mass fraction, (d) temperature, and (e) pressure.

because the partial molar volume difference appears with opposite sign in the species  $A$  mass flux vector. This change in sign of the skewness factor occurs for simulation run 4 (Table V) due to choosing 3-methylhexane to be denoted species  $B$ . Also note that although non-Gaussian scalar statistics can, in some cases, be related to inertial range scalar intermittency,<sup>40,41</sup> the present mass fraction asymmetries associated with  $\Delta v_{,\alpha}$  are not indicative of inertial intermittency. The asymmetries noted in Table V are a purely thermodynamic effect resulting from the nonequilibrium Soret diffusion formulation.

#### D. Energy spectra

The final topic for investigation is the spectral content of the various turbulence and thermodynamic variables. Towards this purpose, instantaneous normalized spectra taken

from the stationary states of each of the simulations are depicted in Fig. 7 as a function of the wave number magnitude. The spectra presented include the kinetic energy, the dissipation of kinetic energy, the species  $B$  mass fraction, the temperature, and the pressure. Several observations can be made from this figure. First, the high-wave-number content of all of the spectra appear to be well resolved as indicated by the monotonic decay with increasing  $k$  (except for the pressure spectra which exhibit a very small increase at very high wave numbers for some of the simulations). This provides further evidence as to the accuracy of the simulations and the numerical approach. A second observation is that the form of the normalized spectra appear to be functions of only the flow Reynolds number; i.e., no significant dependence on either the Mach number or the molecular weight ratio is observed. Finally, each of the mass fraction spectra [Fig. 7(c)]

exhibits a peak value which corresponds closely to the peak of the kinetic energy dissipation spectra [Fig. 7(b)]. The convergence of the peaks would seem to suggest that the production of scalar variance due to the pressure gradient through  $J_i^p$  occurs primarily in the small (dissipation) scales of the flow. This is somewhat intuitive since the gradient of the pressure, which is central to the scalar variance production, obviously exhibits larger high-wave-number contributions than does the pressure field itself.

## VI. CONCLUSIONS

Direct numerical simulations were conducted for stationary compressible isotropic turbulent mixtures at supercritical pressures. In particular, binary mixtures of nitrogen with various hydrocarbon species were studied under supercritical thermodynamic conditions relevant to modern diesel and aircraft gas turbine engines. The formulation is based on the compressible form of the Navier–Stokes equations, coupled with total energy and mass fraction transport equations. High pressure fluid behavior is modeled based on a cubic real gas state equation and general forms of the heat and mass flux vectors derived from nonequilibrium thermodynamics. The formulation therefore includes the potential for heat to diffuse due to species concentration gradients or pressure gradients (Dufour effect), as well as the potential for concentrations to diffuse in the presence of temperature or pressure gradients (Soret effect).

Simulation parameters were chosen to study the effects of the molecular weight ratio, turbulence Reynolds number, and the turbulence Mach number on the long time behavior of the species mass fraction distributions. It was observed that in all cases the mass fraction, rather than undergoing the “typical” (low pressure) exponential decay, achieves stationary statistics characterized by nonzero variance at sufficiently long times. These states are independent of the initial mass fraction conditions, and occur even when the binary species are initially perfectly premixed. In these premixed cases, the initial effect of the Soret diffusion is to “anti-diffuse” the mixture—a phenomenon which is impossible under purely Fickian diffusion. An analysis of the scalar variance budget revealed that the long time stationary scalar states are made possible by a balance between Fickian dissipation effects and a production mechanism involving the pressure-gradient-dependent term of the Soret diffusion. This production mechanism is made possible by a persistent correlation between the pressure and mass fraction gradients. On the other hand, although the temperature gradient term of the Soret diffusion is of significant magnitude compared to the total mass flux vector, its average effect on the scalar variance budget is essentially negligible due to an absence of correlation between the temperature and mass fraction gradients. In contrast, Dufour heat diffusion was found to be essentially negligible when compared to the Fourier heat flux for the simulation parameters under consideration.

The simulation results were then analyzed to elucidate the statistical forms of the stationary mass fraction distributions. It was observed that the long time scalar variance magnitude is an increasing function of both the molecular weight

ratio and the turbulence Mach number; however, the magnitudes decrease with increasing turbulence Reynolds number due to the diminishing influence of molecular diffusion. Probability density functions of the mass fraction were examined and found to be characterized by larger than Gaussian flatness factors and by substantial skewness factors. The asymmetries in the distributions were attributed to the mass fraction dependence of the partial molar volume difference appearing in the pressure gradient dependent term of the Soret diffusion vector. Finally, the mass fraction energy spectra were observed to display peak amplitudes at wave numbers corresponding to the peak of the kinetic energy dissipation spectra. It was concluded that the production of scalar fluctuations occurs primarily in the small scales of the turbulence.

## ACKNOWLEDGMENTS

Computational resources were provided by the JPL/Caltech Supercomputing Project funded by the NASA Offices of Earth Science, Aeronautics, and Space Science. Additional resources were provided by the Division of Computing and Information Technology at Clemson University.

## APPENDIX A: MIXING RULES

The mixing rules recommended by Harstad *et al.*<sup>12</sup> are

$$A_{\alpha\beta} = 0.457236(\mathfrak{R}T_{\alpha\beta}^c)^2[1 + C_{\alpha\beta}(1 - \sqrt{T/T_{\alpha\beta}^c})]^2/p_{\alpha\beta}^c, \quad (\text{A1})$$

$$B_{\alpha} = 0.077796 \mathfrak{R}T_{\alpha\alpha}^c/p_{\alpha\alpha}^c, \quad (\text{A2})$$

$$C_{\alpha\beta} = 0.37464 + 1.54226\Omega_{\alpha\beta} - 0.26992\Omega_{\alpha\beta}^2, \quad (\text{A3})$$

where the superscript *c* refers to critical properties (i.e.,  $T/T^c$  is the “reduced” temperature). The diagonal elements of the “critical matrices” are equal to their pure substance counterparts; i.e.,  $T_{\alpha\alpha}^c = T_{\alpha}^c$ ,  $p_{\alpha\alpha}^c = p_{\alpha}^c$ , and  $\Omega_{\alpha\alpha} = \Omega_{\alpha}$  where  $\Omega$  is the acentric factor of species  $\alpha$ . The off-diagonal elements are evaluated using additional mixing rules:

$$T_{\alpha\beta}^c = \sqrt{T_{\alpha\alpha}^c T_{\beta\beta}^c}(1 - k_{\alpha\beta}), \quad p_{\alpha\beta}^c = Z_{\alpha\beta}^c(\mathfrak{R}T_{\alpha\beta}^c/V_{\alpha\beta}^c), \quad (\text{A4})$$

$$V_{\alpha\beta}^c = \frac{1}{8}[(V_{\alpha\alpha}^c)^{1/3} + (V_{\beta\beta}^c)^{1/3}]^3, \quad Z_{\alpha\beta}^c = \frac{1}{2}(Z_{\alpha\alpha}^c + Z_{\beta\beta}^c),$$

$$\Omega_{\alpha\beta} = \frac{1}{2}(\Omega_{\alpha\alpha} + \Omega_{\beta\beta}), \quad (\text{A5})$$

where the diagonal elements of each of the above symmetric matrices are also equal to the pure substance values. The binary interaction parameter,  $k_{\alpha\beta}$ , is a function of the species being considered and is taken to be  $k_{\alpha\beta} = 0.1$  for  $\alpha \neq \beta$  and  $k_{\alpha\alpha} = 0$  for the binary mixtures addressed in this study.

## APPENDIX B: THERMODYNAMIC FUNCTIONS

In order to ensure self-consistency, all of the thermodynamic parameters of the flow should be calculated from the same equation of state. For the present fluid dynamics simulations the variables of interest are the molar enthalpy ( $H$ ), the constant pressure molar heat capacity ( $C_p$ ), the partial molar enthalpy ( $H_{,\alpha}$ ), the partial molar volume ( $V_{,\alpha}$ ), the

mass diffusion factor ( $\alpha_d$ ), and the speed of sound ( $a_s$ ). Each of these functions can be obtained through various derivatives and functions of the Gibbs energy:<sup>1,29</sup>

$$H = H^0 + pV - \sum_{\alpha} X_{\alpha} \mathfrak{R}T + K_1 \left( \mathcal{A}_m - T \frac{\partial \mathcal{A}_m}{\partial T} \right), \quad (\text{B1})$$

$$C_p = C_p^0 - T \frac{(\partial p / \partial T)_{V,X}^2}{(\partial p / \partial V)_{T,X}} - \sum_{\alpha} X_{\alpha} \mathfrak{R} - T \frac{\partial^2 \mathcal{A}_m}{\partial T^2} K_1, \quad (\text{B2})$$

where:

$$\left( \frac{\partial p}{\partial T} \right)_{V,X} = \sum_{\alpha} X_{\alpha} \mathfrak{R} / (V - \mathcal{B}_m) - (\partial \mathcal{A}_m / \partial T) / (V^2 + 2V\mathcal{B}_m - \mathcal{B}_m^2), \quad (\text{B3})$$

$$\left( \frac{\partial p}{\partial V} \right)_{T,X} = \frac{-\sum_{\alpha} X_{\alpha} \mathfrak{R}T}{(V - \mathcal{B}_m)^2} \left[ 1 - 2\mathcal{A}_m \left\{ \mathfrak{R}T(V + \mathcal{B}_m) \times \left( \frac{V}{V - \mathcal{B}_m} + \frac{\mathcal{B}_m}{V + \mathcal{B}_m} \right)^2 \right\}^{-1} \right], \quad (\text{B4})$$

$$K_1 = \frac{1}{2\sqrt{2}\mathcal{B}_m} \ln \left[ \frac{V + (1 - \sqrt{2})\mathcal{B}_m}{V + (1 + \sqrt{2})\mathcal{B}_m} \right], \quad (\text{B5})$$

$$V_{,\alpha} = \frac{-1}{(\partial p / \partial V)_{T,X}} \left[ \frac{\mathfrak{R}T}{V - \mathcal{B}_m} + \frac{\mathfrak{R}T\mathcal{B}_{\alpha}}{(V - \mathcal{B}_m)^2} + \frac{2\mathcal{A}_m(V - \mathcal{B}_m)\mathcal{B}_{\alpha}}{(V^2 + 2V\mathcal{B}_m - \mathcal{B}_m^2)^2} - \frac{2\sum_{\beta} \mathcal{A}_{\alpha\beta} X_{\beta}}{V^2 + 2V\mathcal{B}_m - \mathcal{B}_m^2} \right], \quad (\text{B6})$$

$$H_{,\alpha} = H_{\alpha}^0 + pV_{,\alpha} - \mathfrak{R}T + \left( \mathcal{A}_m - T \frac{\partial \mathcal{A}_m}{\partial T} \right) \frac{V_{,\alpha} - V\mathcal{B}_{\alpha} / \mathcal{B}_m}{V^2 + 2V\mathcal{B}_m - \mathcal{B}_m^2} + K_1 \left[ \frac{\partial \mathcal{A}_m}{\partial X_{\alpha}} - T \frac{\partial^2 \mathcal{A}_m}{\partial X_{\alpha} \partial T} - \left( \mathcal{A}_m - T \frac{\partial \mathcal{A}_m}{\partial T} \right) \frac{\mathcal{B}_{\alpha}}{\mathcal{B}_m} \right]. \quad (\text{B7})$$

In the above,  $H_{\alpha}^0$  is the pure substance reference enthalpy of species  $\alpha$ . The mass diffusion factor  $\alpha_d$  is a thermodynamic function given by  $\alpha_d = 1 + X_{\alpha} \ln(\phi_{\alpha}) / \partial X_{\alpha}$ , where  $\phi_{\alpha}$  are the fugacity coefficients (independent of which species is chosen in the evaluation) and has the form

$$\alpha_d = 1 + X_A X_B \left\{ \frac{\mathfrak{R}T}{(\partial p / \partial V)_{T,X}} \left( \frac{1}{\mathcal{B}_m^2} \right) \left[ \frac{\mathcal{B}_B - \mathcal{B}_A}{V - \mathcal{B}_m} + \frac{\mathcal{B}_A \partial \mathcal{A}_m / \partial X_B - \mathcal{B}_B \mathcal{A}_m / \partial X_A}{\mathfrak{R}T(V^2 + 2V\mathcal{B}_m - \mathcal{B}_m^2)} \right]^2 + K_2 \right\}, \quad (\text{B8})$$

with

$$K_2 = \left( \frac{\mathcal{B}_B - \mathcal{B}_A}{\mathcal{B}_m} \right)^2 + \frac{2}{\mathfrak{R}T} \left( \frac{K_1}{\mathcal{B}_m^2} \right) (\mathcal{A}_{BB} \mathcal{B}_A + \mathcal{A}_{AA} \mathcal{B}_B - 2\mathcal{A}_{AB} \mathcal{B}_A \mathcal{B}_B). \quad (\text{B9})$$

Finally, for real fluids the speed of sound is  $a = (\rho \kappa_s)^{-1/2}$ , where the isentropic compressibility is  $\kappa_s = \kappa_T - VT\alpha_v^2 / C_p$ , and the expansivity ( $\alpha_v$ ) and the isothermal compressibility ( $\kappa_T$ ) are expressed by

$$\alpha_v = \frac{-(\partial p / \partial T)_{V,X}}{V(\partial p / \partial V)_{T,X}}, \quad \kappa_T = \frac{-1}{V(\partial p / \partial V)_{T,X}}. \quad (\text{B10})$$

Finally, miscellaneous relations used above are

$$\frac{\partial \mathcal{A}_m}{\partial X_{\alpha}} = 2 \sum_{\beta} \mathcal{A}_{\alpha\beta} X_{\beta}, \quad (\text{B11})$$

$$\frac{\partial \mathcal{A}_m}{\partial T} = -\frac{1}{T} \sum_{\alpha} \sum_{\beta} X_{\alpha} X_{\beta} \mathcal{A}_{\alpha\beta} G_{\alpha\beta}, \quad (\text{B12})$$

$$\frac{\partial^2 \mathcal{A}_m}{\partial X_{\alpha} \partial T} = \frac{-2}{T} \sum_{\beta} \mathcal{A}_{\alpha\beta} G_{\alpha\beta} X_{\beta}, \quad (\text{B13})$$

$$\frac{\partial^2 \mathcal{A}_m}{\partial T^2} = \frac{0.457236 \mathfrak{R}^2}{2T} \sum_{\alpha} \sum_{\beta} X_{\alpha} X_{\beta} C_{\alpha\beta} \times (1 + C_{\alpha\beta}) \frac{T_{\alpha\beta}^c}{P_{\alpha\beta}^c} \sqrt{\frac{T_{\alpha\beta}^c}{T}}, \quad (\text{B14})$$

$$G_{\alpha\beta} = \frac{C_{\alpha\beta} \sqrt{T / T_{\alpha\beta}^c}}{1 + C_{\alpha\beta} (1 - \sqrt{T / T_{\alpha\beta}^c})}. \quad (\text{B15})$$

## APPENDIX C: TEMPERATURE CURVE FIT

A cubic real gas state equation must in general be solved iteratively to get both the temperature and pressure simultaneously (given the density, internal energy, and mass fractions). However, in order to avoid costly iterations, a highly accurate fit was obtained for the specific internal energy of the mixture ( $e_i$ ) over the entire state space of interest:

$$\left( \frac{e_i - e_L}{e_U - e_L} \right) = C_1 \left( \frac{T - T_L}{T_U - T_L} \right) + C_2 \left( \frac{T - T_L}{T_U - T_L} \right)^2, \quad (\text{C1})$$

which can be solved explicitly for the temperature. In the above expression,

$$\left( \frac{e_L - e^{(1)}}{e^{(2)} - e^{(1)}} \right) = C_3 \left( \frac{\rho - \rho_L}{\rho_U - \rho_L} \right) + C_4 \left( \frac{\rho - \rho_L}{\rho_U - \rho_L} \right)^2, \quad (\text{C2})$$

$$\left( \frac{e_U - e^{(3)}}{e^{(4)} - e^{(3)}} \right) = C_5 \left( \frac{\rho - \rho_L}{\rho_U - \rho_L} \right) + C_6 \left( \frac{\rho - \rho_L}{\rho_U - \rho_L} \right)^2, \quad (\text{C3})$$

where the subscripts  $L$  and  $U$  correspond to the lower and upper limits of the parameter space, respectively. Finally, the four remaining internal energy functions,  $e^{(1)}(Y_B; T_L, \rho_L)$ ,  $e^{(2)}(Y_B; T_L, \rho_U)$ ,  $e^{(3)}(Y_B; T_U, \rho_L)$ , and  $e^{(4)}(Y_B; T_U, \rho_U)$ , are

$$\left( \frac{e^{(\alpha)} - e_L^{(\alpha)}}{e_U^{(\alpha)} - e_L^{(\alpha)}} \right) = C_7^{(\alpha)} Y_B + C_8^{(\alpha)} Y_B^2; \quad \alpha = 1, 2, 3, 4. \quad (\text{C4})$$

In practice each of the parameters  $C_1 \rightarrow C_8$  is obtained by a least mean square error (LMSE) solution.

The procedure for applying the curve fit is as follows. First, a range of temperature, mass fraction, and pressure (and therefore density) is input which encompasses the thermodynamic state space under consideration. Then the eight constants  $C_7^{(\alpha)}$  and  $C_8^{(\alpha)}$  are determined using the LMSE analysis. This allows the  $e_L$  and  $e_U$  coefficients ( $C_3, C_4, C_5, C_6$ ) to be calculated, again using LMSE. Fi-

nally, another separate application of the LMSE procedure determines the remaining coefficients  $C_1$  and  $C_2$ . The final curve fit Eq. (C1) can then be written in forms which are explicit in either the temperature or the internal energy. The fit can therefore be used to determine both the internal energy during initialization (for consistency), as well as to calculate the temperature from the internal energy during each time step.

The entire curve fitting process is performed during the initialization of the code automatically and requires negligible computational effort. Furthermore, the state space range can be checked dynamically during each simulation. If this range ever extends beyond the input range the curve fit is simply recalculated. Application of the procedure was found to produce highly accurate fits for the temperature as a function of the internal energy for all of the cases considered in this study. For each case, the thermodynamic state space chosen for the fit was  $0 \leq Y_B \leq 1$ ,  $500 \text{ K} \leq T \leq 1250 \text{ K}$ , and  $25 \text{ atm} \leq p \leq 100 \text{ atm}$ . The average relative errors for the temperature estimates when compared to the "exact" Peng–Robinson temperature are 0.57% for nitrogen with heptane, 0.21% for heptane with 3-methylhexane, and 0.55% for nitrogen with dodecane over the entire state space ranges.

- <sup>1</sup>R. C. Reid, J. M. Prausnitz, and B. E. Poling, *The Properties of Gases and Liquids* (McGraw-Hill, New York, 1987).
- <sup>2</sup>T. Kamimoto and H. Kobayashi, "Combustion processes in diesel engines," *Prog. Energy Combust. Sci.* **17**, 163 (1991).
- <sup>3</sup>A. H. Lefebvre, *Gas Turbine Combustion* (Taylor and Francis, Ann Arbor, MI, 1998).
- <sup>4</sup>S. D. Givler and J. Abraham, "Supercritical droplet vaporization and combustion studies," *Prog. Energy Combust. Sci.* **22**, 1 (1996).
- <sup>5</sup>S. R. De Groot and P. Mazur, *Non-Equilibrium Thermodynamics* (Dover, New York, 1984).
- <sup>6</sup>O. E. Tewfik, E. R. G. Eckert, and C. J. Shirliffe, "Thermal diffusion effects on energy transfer in a turbulent boundary layer with helium injection," in *Proceedings of the 1962 Heat Transfer and Fluid Mechanics Institute*, pp. 42–61.
- <sup>7</sup>O. E. Tewfik and J. W. Yang, "The thermodynamic coupling between heat and mass transfer in free convection with helium injection," *Int. J. Heat Mass Transf.* **6**, 915 (1963).
- <sup>8</sup>E. W. Curtis and P. V. Farrell, "A numerical study of high-pressure droplet vaporization," *Combust. Flame* **90**, 85 (1992).
- <sup>9</sup>K. G. Harstad and J. Bellan, "Isolated fluid oxygen drop behavior in fluid hydrogen at rocket chamber pressures," *Int. J. Heat Mass Transf.* **41**, 3537 (1998).
- <sup>10</sup>K. G. Harstad and J. Bellan, "Interactions of fluid oxygen drops in fluid hydrogen at rocket chamber pressures," *Int. J. Heat Mass Transf.* **41**, 3551 (1998).
- <sup>11</sup>K. G. Harstad and J. Bellan, "An all pressure fluid-drop model applied to a binary mixture: Heptane in nitrogen" (in press).
- <sup>12</sup>K. G. Harstad, R. S. Miller, and J. Bellan, "Efficient high pressure state equations," *AIChE J.* **43**(6), 1605 (1997).
- <sup>13</sup>J. A. Newman and T. A. Brzustowski, "Behavior of a liquid jet near the thermodynamic critical region," *AIAA J.* **9**, 1595 (1971).
- <sup>14</sup>J. Gotz and A. K. Gupta, "Fuel-air mixing under simulated high pressure and high temperature conditions," *AIAA Pap. No.* 98-0269 (1998).
- <sup>15</sup>H. McCann, E. Jepsen, and T. E. Parker, "Near-field droplet size measurements for a diesel spray at high background gas pressure," *AIAA Pap. No.* 98-0150 (1998).
- <sup>16</sup>J. Labs and T. E. Parker, "Droplet size and volume fraction measurements in diesel sprays," *AIAA Pap. No.* 99-0331 (1999).
- <sup>17</sup>B. Chehroudi, D. Talley, and E. Coy, "Initial growth rate and visual characteristics of a round jet into a sub- to supercritical environment of relevance to rocket, gas turbine, and diesel engines," *AIAA Pap. No.* 99-0206 (1999).
- <sup>18</sup>J. C. Lasheras, E. Villermaux, and E. J. Hopfinger, "Break up and atomization of a round water jet by a high-speed annular air jet," *J. Fluid Mech.* **357**, 351 (1998).
- <sup>19</sup>R. S. Miller, C. K. Madnia, and P. Givi, "Numerical simulation of non-circular jets," *Comput. Fluids* **24**, 1 (1995).
- <sup>20</sup>J. C. Oefelein and V. Yang, "Analysis of transcritical spray phenomena in turbulent mixing layers," *AIAA Pap. No.* 96-0085 (1996).
- <sup>21</sup>J. C. Oefelein and V. Yang, "Analysis of hydrogen-oxygen mixing and combustion processes at high-pressures," *AIAA Pap. No.* 97-0798 (1997).
- <sup>22</sup>R. S. Miller, K. G. Harstad, and J. Bellan, "Direct numerical simulation of a supercritical mixing layer," *AIAA Pap. No.* 2000-0195 (2000).
- <sup>23</sup>R. S. Miller, K. G. Harstad, and J. Bellan, "Direct numerical simulation of supercritical fluid mixing layers applied to heptane-nitrogen" (submitted).
- <sup>24</sup>S. B. Pope, "Pdf methods for turbulent reacting flows," *Prog. Energy Combust. Sci.* **11**, 119 (1985).
- <sup>25</sup>H. Chen, S. Chen, and R. H. Kraichnan, "Probability distribution of a stochastically advected scalar field," *Phys. Rev. Lett.* **63**, 2657 (1989).
- <sup>26</sup>S. B. Pope, "Mapping closures for turbulent mixing and reaction," *Theor. Comput. Fluid Dyn.* **2**, 255 (1991).
- <sup>27</sup>R. S. Miller, S. H. Frankel, C. K. Madnia, and P. Givi, "Johnson-Edgeworth translation for probability modeling of binary mixing in turbulent flows," *Combust. Sci. Technol.* **91**, 21 (1993).
- <sup>28</sup>J. Keizer, *Statistical Thermodynamics of Nonequilibrium Processes* (Springer Verlag, New York, 1987).
- <sup>29</sup>K. Denbigh, *The Principles of Chemical Equilibrium* (Cambridge University Press, Cambridge, 1981).
- <sup>30</sup>S. Sarman and D. J. Evans, "Heat flow and mass diffusion in binary Lennard-Jones mixtures," *Phys. Rev. A* **45**, 2370 (1992).
- <sup>31</sup>S. Chapman and T. G. Cowling, *The Mathematical Theory of Non-Uniform Gases* (Cambridge University Press, Cambridge, 1970).
- <sup>32</sup>S. Kida and S. A. Orszag, "Energy and spectral dynamics in forced compressible turbulence," *J. Sci. Comput.* **5**, 85 (1990).
- <sup>33</sup>C. A. Kennedy and M. H. Carpenter, "Several new numerical methods for compressible shear-layer simulations," *Appl. Numer. Math.* **14**, 397 (1994).
- <sup>34</sup>R. S. Miller and J. Bellan, "Direct numerical simulation and subgrid analysis of a transitional droplet laden mixing layer," *Phys. Fluids* **12**, 650 (2000).
- <sup>35</sup>R. S. Miller and J. Bellan, "Direct numerical simulation of a confined three-dimensional gas mixing layer with one evaporating hydrocarbon-droplet laden stream," *J. Fluid Mech.* **384**, 293 (1999).
- <sup>36</sup>S. Lee, S. K. Lele, and P. Moin, "Eddy shocklets in decaying compressible turbulence," *Phys. Fluids A* **3**, 657 (1991).
- <sup>37</sup>R. S. Miller and J. Bellan, "On the validity of the assumed pdf method for modeling binary mixing/reaction of evaporated vapor in gas/liquid-droplet turbulent shear flow," in *Proceedings of the 27th Symposium (International) on Combustion* (1998), pp. 1065–1072.
- <sup>38</sup>V. Eswaran and S. B. Pope, "Direct numerical simulations of the turbulent mixing of a passive scalar," *Phys. Fluids* **31**, 506 (1988).
- <sup>39</sup>R. S. Miller, F. A. Jaber, C. K. Madnia, and P. Givi, "The structure and the small-scale intermittency of passive scalars in homogeneous turbulence," *J. Sci. Comput.* **10**, 151 (1995).
- <sup>40</sup>B. Castaing, G. Gunaratne, F. Heslot, L. Kadanoff, A. Libchaber, S. Thomae, X. Z. Wu, S. Zaleski, and G. Zanetti, "Scaling of hard thermal turbulence in Rayleigh-Benard convection," *J. Fluid Mech.* **204**, 1 (1989).
- <sup>41</sup>F. A. Jaber, R. S. Miller, C. K. Madnia, and P. Givi, "Non-Gaussian scalar statistics in homogeneous turbulence," *J. Fluid Mech.* **313**, 241 (1996).